ACCSCIENCE PUBLISHING

Materials Science in Additive Manufacturing

ORIGINAL RESEARCH ARTICLE

Topology optimization for negative Poisson's ratio metamaterials with geometric curvature control

Kaixian Liang, Chengxiang Liu, and Jikai Liu*

Key Laboratory of High Efficiency and Clean Mechanical Manufacture (Ministry of Education), School of Mechanical Engineering, Shandong University, Jinan, Shandong, China

Abstract

Metamaterials with a negative Poisson's ratio (NPR) exhibit unique auxetic deformation mechanism that enables superior energy absorption and mechanical resilience. Topology optimization (TO) can effectively generate microstructures with NPR characteristics, but conventional optimized designs often suffer from sharp corners and stress concentrations, which compromise durability and limit multicycle energy absorption. To address this issue, we introduced a boundary-fitting derivable geodesics-coupled TO (B-DGTO) framework to construct explicit curvature constraints into the optimization process, ensuring smooth boundaries and more uniform stress distribution with optimal NPR properties. In numerical example and experiment, we provided different types of 2D/3D NPR microstructures under curvature control to demonstrate the versatility of the proposed approach. These results confirm that the curvature constraint significantly improves the stress distribution of NPR microstructures and enhances their robustness and reliability under repeated loading. This study highlights curvature-constrained TO as a general and practical strategy for developing durable NPR metamaterials with superior energy dissipation performance.

Keywords: NPR metamaterials; Topology optimization; Curvature constraint; Energy absorption

***Corresponding author:**
Jikai Liu
(jikai_liu@sdu.edu.cn)

Citation: Liang K, Liu C, Liu J. Topology optimization for negative Poisson's ratio metamaterials with geometric curvature control. *Mater Sci Add Manuf*. 2026;5(2):025440103. doi: 10.36922/MSAM025440103

Received: October 27, 2025

Revised: November 26, 2025

Accepted: December 3, 2025

Published online: February 13, 2026

1. Introduction

Mechanical metamaterials with negative Poisson's ratios (NPR)[1-3] exhibit lateral expansion under tension and contraction under compression. This unusual behavior imparts superior properties such as structural toughness,[4,5] acoustic tenability,[6-8] thermal conductivity adjustability,[9-11] and enhanced impact resistance.[12-14] Consequently, NPR metamaterials hold great potential in applications ranging from vibration and noise control to protective devices and aerospace engineering.

Current design methodologies for NPR metamaterials can be broadly categorized into three classes: Beam-rod stacking, origami/kirigami-inspired, and topology optimization (TO). The beam-rod stacking method relies heavily on designers' experience and has been widely studied, yielding many classical NPR metamaterial configurations.[2,3] Origami/Kirigami-inspired strategies have also been explored.[15-17] However, the intrinsic

geometric constraints of origami patterns—such as creases and vertices—significantly limit the design flexibility of NPR metamaterials. In contrast, TO formulates the design task as a mathematical optimization problem, enabling systematic exploration of complex geometries and facilitating the discovery of novel NPR configurations that surpass traditional intuition-driven designs.

Many classical TO methods have been established over the past decades.[18-22] The pioneering work of Sigmund[23] incorporated TO into material design by proposing an inverse homogenization framework to realize NPR microstructures. Building upon this foundation, subsequent studies have developed isotropic NPR metamaterials that exhibit uniform auxetic behavior in all loading directions[24-26] and orthotropic designs that enhance energy absorption along specific axes.[27,28] More recently, chiral microstructures have been developed, characterized by high deformability, low shear stiffness, and retention of the NPR characteristic under large strains.[29-31] For NPR metamaterials designed through TO,[32,33] their extraordinary energy absorption capability is primarily governed by the dimensions and arrangement of the embedded flexible hinges (known as "spring joint" by some researchers). In practical applications, such energy-absorbing microstructures are often expected to withstand repeated loading cycles. However, the flexible hinges represent the most vulnerable regions of microstructures, where stress concentration is prone to occur. Consequently, the strength and durability of these hinges play a decisive role in determining whether the NPR microstructures can be reliably reused in multiple energy absorption cycles. Bernard *et al.*[34] studied the influence of beams with different cross-sections on microstructure performance, which can reduce the presence of geometrically sharp regions in microstructures. Ni *et al.*[35] proposed a two-scale TO framework that incorporates high-cycle fatigue constraints to improve the stress distribution of hierarchical structures, thereby mitigating premature failure at the microscale. Although this approach effectively redistributes stresses, the optimization process does not alter the intrinsic geometry of the microstructures. As a result, sharp features in the microstructure are retained, preserving the most susceptible sites for stress concentration and fatigue damage, especially when manufacturing imperfections are considered. Sharp microstructural features are particularly undesirable in additive manufacturing, as they are prone to fabrication defects, residual stresses, and geometric inaccuracies, which further amplify local stress concentrations and significantly increase the risk of premature failure under cyclic loading. Therefore, a new optimization strategy that reinforces the weak regions of NPR microstructures (typically the flexible hinges and sharp features) is required to ensure reliable performance under repeated loading cycles.

In this paper, we propose a curvature constraint strategy based on DGTO to address the sharpness issue of flexible hinges, thus increasing the reusable cycles of NPR metamaterials.[36-38] B-DGTO is a framework that we previously developed to convert the density field into a signed distance function (SDF). This framework has the following advantages:

(i) Geometrical equivalence: B-DGTO ensures that the density field and SDF are geometrically equivalent, so the SDF's geometric information can be used on top of the density field, improving evaluation accuracy.
(ii) Accurate curvature calculation: The SDF provides precise calculation of boundary curvatures,[39] a feature missing in density methods, helping reduce sharp curvatures and stress concentrations in flexible hinge.
(iii) Differentiability: The conversion from the density field to the SDF is fully differentiable, preventing local optimal during optimization.

2. Materials and methods

2.1. Asymptotic homogenization of microstructures

A large number of symbols are used in this work, and their meanings can be found in Appendix Table 1. The material properties of periodic microstructures are predicted by the asymptotic homogenization method.[23] The effective elasticity tensors D^H of microstructures can be written as (3 × 3 matrix form for 2D problem and 6 × 6 matrix form for 3D problem):

$$\mathrm{D}^H = \begin{bmatrix} D^H_{1111} & D^H_{1122} & D^H_{1112} \\ D^H_{2211} & D^H_{2222} & D^H_{2212} \\ D^H_{1211} & D^H_{1222} & D^H_{1212} \end{bmatrix} \tag{I}$$

D^H_{ijkl} in Equation I can be calculated by the energy form:

$$D^H_{ijkl} = \frac{1}{|Y|}\int_Y D_{pqrs}\left(\varepsilon^{0(ij)}_{pq} - \varepsilon^{*(ij)}_{pq}\right)\left(\varepsilon^{0(kl)}_{rs} - \varepsilon^{*(kl)}_{rs}\right)dY \tag{II}$$

Where Y is the volume of the periodic unit cell; D_{pqrs} represents the elastic tensor when the unit cell is completely solid; $\varepsilon^{0(ij)}_{pq}$ represents three independent unit strains for testing microstructural properties (corresponding to six independent unit test strains in 3D problem); $\varepsilon^{*(ij)}_{pq}$ denotes the response strains, which can be calculated by:

$$\int_Y D_{ijpq}\varepsilon_{ij}\left(\upsilon^{ij}\right)\varepsilon^{*(ij)}_{pq}dY = \int_Y D_{ijpq}\varepsilon_{ij}\left(\upsilon^{ij}\right)\varepsilon^{0(ij)}_{pq}dY, \quad \forall \upsilon \in \tilde{V} \tag{III}$$

Where υ is the virtual displacement and $\tilde{V} = \{\upsilon : \upsilon \text{ is Y-periodic}\}$ in Equation III.

The finite element form of Equation II can be rewritten as:

$$D_{ijkl}^{H}=\frac{1}{|Y|}\sum_{n=1}^{k}\left(\mathrm{u}_{n}^{A(ij)}\right)^{\top}\mathrm{k}_{n}\mathrm{u}_{n}^{A(kl)} \quad \text{(IV)}$$

Where the element displacement u_{n}^{A} is used to replace the superimposed strain fields $\left(\varepsilon_{pq}^{0}-\varepsilon_{pq}^{*}\right)$ in Equation II. k_{n} is the element stiffness matrix, and it can be obtained by interpolating with design variables:

$$\mathrm{k}_{n}=\left[E_{micro}^{\min}+\tilde{\tilde{\rho}}_{n}^{p}\left(E_{micro}^{0}-E_{micro}^{\min}\right)\right]\mathrm{k}_{micro}^{0} \quad \text{(V)}$$

In Equation V, $E_{micro}^{\min}=1\mathrm{e}-9$ is used to avoid computational singularity; E_{micro}^{0} is the elastic modulus of based material; $\tilde{\tilde{\rho}}$ is the physical density, which is obtained by applying the PDE filter and Heaviside projection to the design variable ρ; k_{micro}^{0} is the element stiffness matrix of based material; p=3 serves as the penalization factor to penalize intermediate densities.

2.2. Curvature constraint for NPR metamaterials by B-DGTO framework

Imposing curvature constraints on NPR metamaterials can smooth sharp domain, thereby mitigating stress concentration and reducing failure probability under high-cycle loading. In pixel-based density field, the absence of explicit boundary information limits the extraction and control of boundary curvature. In contrast, our previously proposed B-DGTO framework transforms the density field into a SDF φ that possesses the property $|\nabla\varphi|=1$, thereby facilitating curvature control. Here, we provide a brief review of the B-DGTO framework.

B-DGTO framework for curvature constraint is mainly divided into seven steps, as shown in Figure 1. It mainly converts the density field into SDF with precise boundary through the heat method.[40]

As shown in Figure 1, all domain V encompasses both the blank domain and the design domain D. In Step I, by performing a few optimization iterations on the initial density guess, a microstructural density field with a preliminary profile can be obtained. To ensure that curvature constraint can also be imposed at the junctions of periodic microstructures, the stitched density field $\hat{\rho}$ is obtained through the boundary stitching in Step II. It is noteworthy that the stitched density field $\hat{\rho}$ is only used for curvature calculation, whereas the performance computation (finite element analysis) and optimization process are still conducted based on the density field $\tilde{\tilde{\rho}}$. In Step III, the thermal conductivity matrix Q associated with the density field $\hat{\rho}$ is constructed by:

$$\mathrm{Q}=\sum_{i=1}^{N}\left(\hat{\rho}_{i}\left(h_{0}-h_{\min}\right)+h_{\min}\right)\mathrm{A}_{i}^{\mathrm{T}}\mathrm{Q}_{0}\mathrm{A}_{i} \quad \text{(VI)}$$

Where h_0 = 1 is the coefficient of thermal conductivity, and h_{min} = 1e−3 is used to ensure the stability of numerical calculations. A_{i} is the assembly matrix. Q_{0} is the elemental transient thermal conductivity matrix.[41] One applies heat load b with an all-one vector and solves the following finite element form of the heat diffusion equation to obtain the temperature field T:

$$\mathrm{QT}=\mathrm{b} \quad \text{(VII)}$$

According to Fourier's law and the continuity of heat flux, the direction of heat flow always points from high temperature to low. Therefore, the ambient with inefficient thermal diffusion employs obviously high temperature, and the temperature gradient is always perpendicular to the structural boundary.

In Step IV, the SDF φ is obtained by solving the following finite element form of the Poisson equation using normalized temperature gradient $\omega=\nabla\mathrm{T}/|\nabla\mathrm{T}|$ as input:

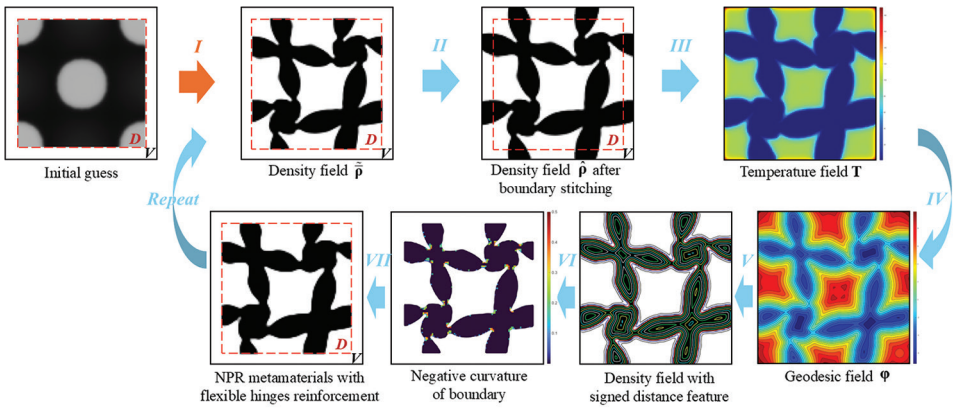

Figure 1. Diagram of the NPR microstructure optimization with curvature constraint generated by SDF
Abbreviations: NPR: Negative Poisson's ratio; SDF: Signed distance function

$$\begin{bmatrix} L_{11} & L_{12} \\ L_{21} & L_{22} \end{bmatrix} \begin{bmatrix} \varphi_1 \\ \varphi_2 \end{bmatrix} = \begin{bmatrix} \nabla \cdot \omega_1 \\ \nabla \cdot \omega_2 \end{bmatrix} \quad \text{(VIII)}$$

Where φ_1 is employed as a Dirichlet boundary condition to ensure that the interpolated density boundary coincides with the 0 isosurface of the SDF. φ_2 is the unknown SDF value. L_{ij} is the block Laplacian matrix corresponding to φ_1 and φ_2. We take the density threshold of 0.5 as the zero isosurface in generating SDF to ensure the geometrical equivalence, since the threshold η=0.5 is employed in the Heaviside projection. In fact, the density threshold can be set to any value within the range of 0.1 to 1 in case of consistency. The implementation mainly relies on a marching cubes style boundary detection and interpolation method. The interpolated zero isosurface of the SDF is then imposed as a Dirichlet boundary condition φ_1, thereby Equation VIII can be rewritten as:

$$L_{12}\,\varphi_2 = \nabla.\omega_1 - L_{11}\,\varphi_1 \quad \text{(IX)}$$

In Step V, the zero isosurface of SDF is geometrically equivalent to the density field, so the signed distance feature is realized on top of the densities. For the derivation processes of Equations VI to IX, we suggest that readers refer to previous studies to gain a more detailed understanding.

The boundary elements of the density field can be easily obtained by:

$$\varphi_b = H\left(\varphi_{-1}^{iso}\right) - H\left(\varphi_1^{iso}\right) \quad \text{(X)}$$

Where $H(.)$ is the Heaviside projection.[42] φ_{-1}^{iso} and φ_1^{iso} represent the −1 and 1 iso-surface of the signed distance field φ. The mean curvature κ and the boundary mean curvature κ_b can be calculated by:

$$\begin{cases} \kappa(\varphi) = \nabla \cdot \left(-\dfrac{\nabla \varphi}{|\nabla \varphi|} \right) \\ \kappa_b = \varphi_b \kappa(\varphi) \end{cases} \quad \text{(XI)}$$

For the flexible hinges in the NPR microstructures, a concave shape indicates a larger negative curvature. Therefore, in Step VI, we need to extract the boundary negative curvature κ_b^N by the sigmoid function:

$$\kappa_b^N = \frac{-\kappa_b}{1 + e^{\beta_s \kappa_b}} \quad \text{(XII)}$$

Moreover, by adopting the P-norm aggregation method,[43] the local curvature constraints are transformed into a global maximum curvature constraint:

$$\delta = \lim_{P \to \infty} \left(\int_D \left(\kappa_b^{(\cdot)} \right)^P \mathrm{d}\Omega \right)^{\frac{1}{P}} \quad \text{(XIII)}$$

In Equations XII and XIII, β_s = 100 and P = 18 is adopted.

Finally, the B-DGTO framework with negative curvature constraint for NPR metamaterials can be built as:

$$\begin{aligned} &\text{Find } \rho = \{\rho_1, \rho_2, \ldots, \rho_n\}^{\mathrm{T}} \\ &\text{Min. } c(\rho) = D_{1122}^H - \alpha^{(k)} \left(D_{1111}^H + D_{2222}^H \right) \\ &s.t. \begin{cases} \int_Y D_{ijpq} \varepsilon_{ij}(\upsilon^{ij}) \varepsilon_{pq}^{*(ij)} dY = \int_Y D_{ijpq} \varepsilon_{ij}(\upsilon^{ij}) \varepsilon_{pq}^{0(ij)} dY, \quad \forall \upsilon \in \tilde{V} \\ \delta(\rho) - \kappa_{\max} \le 0 \\ V(\rho) - f_v V_0 \le 0 \\ \rho \in [0,1] \end{cases} \end{aligned} \quad \text{(XIV)}$$

The optimization objective in Equation XIV is defined to find the NPR microstructure,[44] $\alpha^{(k)}$ is a parameter that decreases with the number of iterations k and gradually reduces the value of to D_{1122}^H achieve NPR. α = 0.8 and k = loop are adopted as the power indices. $\kappa_{\max}$ is maximum allowable negative curvature, V_0 is the whole volume of a unit cell, and f_v is the maximum allowable volume fraction. Step VI strengthens the flexible hinges by solving the above TO problem.

2.3. Sensitivity analysis

In this study, the method of moving asymptote was used to solve the optimization problem; therefore, it is necessary to obtain the derivatives of the objective function and constraint function on the design variables.[45]

For the objective function, its sensitivity analysis can be obtained through the chain rule:

$$\frac{\partial c}{\partial \rho_e} = \frac{\partial D_{1122}^H - \alpha^{(k)} \left(\partial D_{1111}^H + \partial D_{2222}^H \right)}{\partial \tilde{\bar{\rho}}_i} \frac{\partial \tilde{\bar{\rho}}_i}{\partial \bar{\rho}_i} \frac{\partial \bar{\rho}_i}{\partial \rho_e} \quad \text{(XV)}$$

Where $\partial D_{ijkl}^H / \partial \tilde{\bar{\rho}}$ can be obtained by the adjoint method:

$$\frac{\partial D_{ijkl}^H}{\partial \tilde{\bar{\rho}}_i} = \frac{1}{|Y|} p \tilde{\bar{\rho}}_i^{p-1} \left(E_{micro}^0 - E_{micro}^{\min} \right) \left(\mathrm{u}_i^{A(ij)} \right)^{\top} \mathrm{k}_{micro}^0 \mathrm{u}_i^{A(kl)} \quad \text{(XVI)}$$

The remaining parts $\partial \tilde{\bar{\rho}}_i / \partial \bar{\rho}_i$ and $\partial \bar{\rho}_i / \partial \rho_e$ are the sensitivity analysis of Heaviside projection[43] and PDE filter,[46] which can be easily realized.

For the volume constraint, its sensitivity analysis can be written as:

$$\frac{\partial V}{\partial \rho_e} = \frac{\partial V}{\partial \tilde{\bar{\rho}}_i} \frac{\partial \tilde{\bar{\rho}}_i}{\partial \bar{\rho}_i} \frac{\partial \bar{\rho}_i}{\partial \rho_e} \quad \text{(XVII)}$$

Where $\partial V/\partial\tilde{\bar{\rho}}_i = 1$.

The sensitivity analysis of the negative curvature constraint is obtained by the following chain rule:

$$\frac{\partial\delta}{\partial\rho_e} = \frac{\partial\delta}{\partial\kappa_b^N}\frac{\partial\kappa_b^N}{\partial\kappa_b}\frac{\partial\kappa_b}{\partial\varphi}\frac{\partial\varphi}{\partial\rho_e} \tag{XVIII}$$

Where:

$$\begin{cases} \dfrac{\partial\delta}{\partial\kappa_b^N} = \left(\int_D \left(\kappa_b^N\right)^P \mathrm{d}\Omega\right)^{\frac{1}{P}-1}\left(\kappa_b^N\right)^{P-1} \\ \dfrac{\partial\kappa_b^N}{\partial\kappa_b} = \dfrac{-1-e^{-\beta_s\kappa_b}\left(1-\beta\kappa_b\right)}{\left(1+e^{\beta_s\kappa_b}\right)^2} \\ \dfrac{\partial\kappa_b}{\partial\varphi} = \varphi_b\nabla\cdot\left(-\left(|\nabla\varphi|\dfrac{\partial\left(\nabla\varphi\right)}{\partial\varphi} - \left(\dfrac{\nabla\varphi}{|\nabla\varphi|}\cdot\dfrac{\partial\left(\nabla\varphi\right)}{\partial\varphi}\right)\nabla\varphi\right)\Big/|\nabla\varphi|^2\right) \end{cases} \tag{XIX}$$

The last part $\partial\varphi/\partial\rho_e$ is the partial derivative of the SDF with respect to the design variable ρ:

$$\frac{\partial\varphi}{\partial\rho_e} = \frac{\partial\varphi}{\partial\omega_k}\frac{\partial\omega_k}{\partial T_j}\frac{\partial T_j}{\partial\tilde{\bar{\rho}}_i}\frac{\partial\tilde{\bar{\rho}}_i}{\partial\bar{\rho}_i}\frac{\partial\bar{\rho}_i}{\partial\rho_e} \tag{XX}$$

Lagrange multipliers λ_1 and λ_2 are introduced to solve $\partial\varphi/\partial\omega_k$ and $\partial T_j/\partial\tilde{\bar{\rho}}_i$:

$$\begin{cases} \dfrac{\partial\varphi}{\partial\omega_k} = \dfrac{\partial\varphi}{\partial\omega_k} + \lambda_1^{\mathrm{T}}\left(\mathrm{L}\dfrac{\partial\varphi}{\partial\omega_k} - \dfrac{\partial\left(\nabla\cdot\omega\right)}{\partial\omega_k}\right) \\ \dfrac{\partial T_j}{\partial\tilde{\bar{\rho}}_i} = \dfrac{\partial T_j}{\partial\tilde{\bar{\rho}}_i} + \lambda_2^{\mathrm{T}}\left(\dfrac{\partial\mathrm{Q}}{\partial\tilde{\bar{\rho}}_i}\mathrm{T} + \mathrm{Q}\dfrac{\partial\mathrm{T}}{\partial\tilde{\bar{\rho}}_i}\right) \end{cases} \tag{XXI}$$

The remaining parts of $\partial\omega_k/\partial T_j$ and $\partial\mathrm{Q}/\partial\tilde{\bar{\rho}}_i$ can be derived by:

$$\begin{cases} \dfrac{\partial\omega_k}{\partial T_j} = \dfrac{\partial\left(\dfrac{\nabla T_k}{|\nabla T_k|}\right)}{\partial T_j} = \dfrac{\dfrac{\partial\left(\nabla T_k\right)}{\partial T_j}|\nabla T_k| - \nabla T_k\dfrac{\partial\left(|\nabla T_k|\right)}{\partial T_j}}{\left(|\nabla T_k|\right)^2} \\ \dfrac{\partial\mathrm{Q}}{\partial\tilde{\bar{\rho}}_i} = \left(\left(h_0 - h_{\min}\right) + h_{\min}\right)\mathrm{A}_i^{\mathrm{T}}\mathrm{Q}_0\mathrm{A}_i \end{cases} \tag{XXII}$$

2.4. Numerical implementation

The optimization flowchart is shown in Figure 2. The initial guess of the design variables is given in initialization. The objective function is dominated by the tension-compression moduli in the early stage of iterations, which serves to obtain a configuration with the capacity to resist deformation. As iterations increase, the value of $\alpha^{(k)}$ gradually decreases, and Poisson's ratio becomes dominant, thereby generating NPR structures. If the curvature constraint is introduced too early, it will be difficult to generate microstructures with the NPR effect. For this reason, microstructure optimization is performed without curvature constraint in the first 30 iterations. The TO problem is solved by the method of moving asymptote until convergence is achieved, where convergence is defined as the average relative change of the design variables between two iterations falling below 0.001 and all constraints have been satisfied.

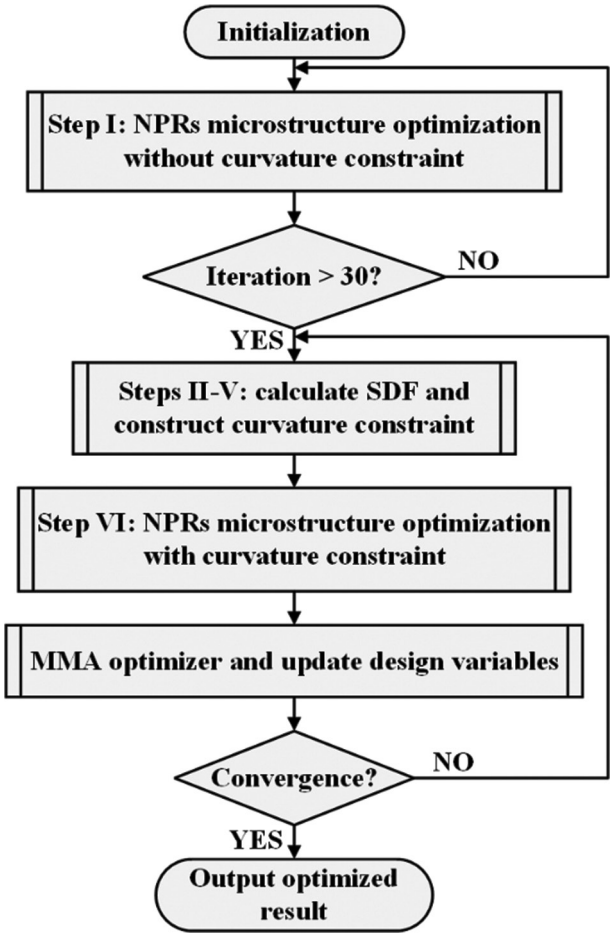

Figure 2. Flowchart of the proposed method
Abbreviations: MMA: Method of moving asymptote; NPR: Negative Poisson's ratio; SDF: Signed distance function

3. Results

We used five numerical example to validate the effectiveness of the proposed method, including 2D isotropic NPR microstructures, 2D anisotropic NPR microstructures, 2D chiral NPR microstructures, and two 3D anisotropic NPR microstructures. The initial guesses for these five cases correspond to Figure 3A-E. The discretization resolution for 2D cases is 100×100, whereas for the 3D cases is 50×50×50. For all initial guesses, two uniform initial

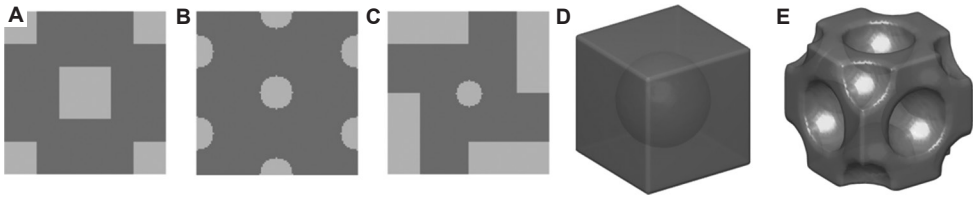

Figure 3. Initial guess for different NPR microstructures for case 1 (A), case 2 (B), case 3 (C), case 4 (D), and case 5 (E)
Abbreviation: NPR: Negative Poisson's ratio

densities were assigned: the dark domains were set to an initial density of 0.5, whereas the light domains were set to an initial density of 0.25.

3.1. 2D case 1: Isotropic NPR microstructures

For 2D case 1, the volume constraint of all isotropic NPR microstructures was set with f_v = 50%. Four comparative scenarios were examined: (i) microstructure without curvature constraint, (ii) microstructure with a negative curvature constraint of κ_{max} = 1, (iii) microstructure with a negative curvature constraint of κ_{max} = 0.8, and (iv) microstructure with a negative curvature constraint of κ_{max} = 0.7. Negative curvature refers to the curvature whose geometry is concave, whereas the absolute value is utilized to build constraints. All negative curvatures are converted to positive values using Equation XII; therefore, all negative curvatures below are described with positive signs.

The optimization results are summarized in Table 1. To save space, we only present the iteration curves of the microstructure with curvature constraint of κ_{max} = 0.8 in Figure 4, and the iterative processes for the remaining examples are analogous to this one. In the early iteration, the microstructure has no NPR effect. At iteration 30, the microstructure demonstrates the NPR effect, whereas a considerable quantity of gray elements remains. The B-DGTO framework with curvature constraint is implemented from this iteration. Subsequent iterations show that the objective function drives the microstructure toward a more pronounced NPR effect, whereas the curvature constraint smooths flexible hinges. However, to strictly satisfy the curvature constraint in the later stage of optimization, many flexible hinges disappear, and the NPR effect is attenuated.

For the NPR microstructure without curvature constraint, the maximum negative curvature reached 2.1. Its geometry contains numerous sharp flexible hinges, which ensure the NPR deformation behavior with a corresponding NPR value of $\mu_{12} = \mu_{21} = -0.58$. However, these sharp, flexible hinges inevitably induce stress concentration during deformation, with a maximum stress of 1.01×10^3 MPa observed in the stress distribution. Such stress concentration hinders the NPR microstructure

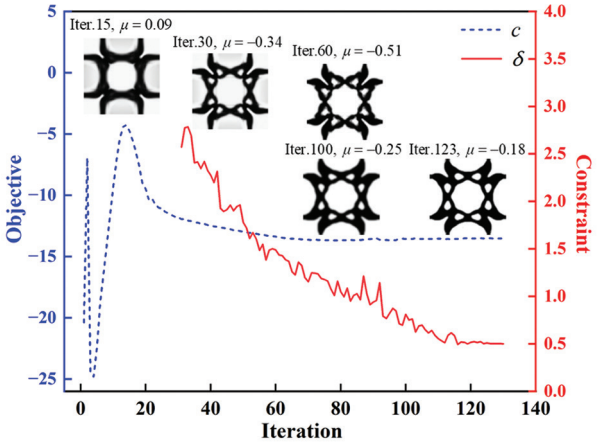

Figure 4. Convergence history of the isotropic NPR microstructure under curvature constraint κ_{max} = 0.8
Abbreviation: NPR: Negative Poisson's ratio

from achieving high-cycle energy absorption. For the NPR microstructures with maximum negative curvature constraints of κ_{max} = 1 and κ_{max} = 0.8, increasing the constraint alleviates the sharpness of the flexible hinges. Under the κ_{max} = 0.8 constraint, flexible hinges are almost eliminated, leading to a Poisson's ratio of $\mu_{12} = \mu_{21} = -0.18$ and a significant reduction in the auxetic effect. For better observation and comparison, the upper limit of the scale bar for stresses was consistently set to 1.04×10^3 MPa. The results show that stronger curvature constraints remarkably reduce stress concentration. Moreover, for isotropic NPR microstructure, curvature constraints also enhance the tensile–compressive stiffness (D_{1111} and D_{2222}), which is consistent with the fact that the weakening of flexible hinges makes the microstructure more resistant to deformation. After applying a curvature constraint of κ_{max} = 0.7, the microstructure transforms into a quasi-zero Poisson's ratio structure. Although its internal stress is further reduced, it no longer presents the NPR effect. It is foreseeable that with further enhanced curvature constraints, the optimized microstructure will no longer exhibit the auxetic effect. For these NPR microstructures, excessive restrictions to curvatures damage the NPR effect since their deformation is highly dependent on the flexibility of hinges.

Table 1. Comparison of isotropic NPR microstructures under different curvature constraints.

Isotropic NPR microstructures	Base cell	Von mises stress distribution under simultaneously applied unit test strains	unite cells	Properties D^H μ_{12} μ_{21}
Without curvature constraint κ_{max}=2.1	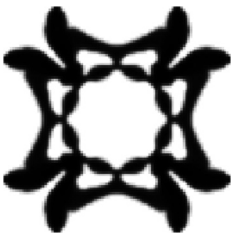	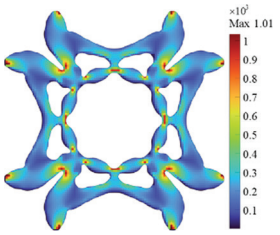	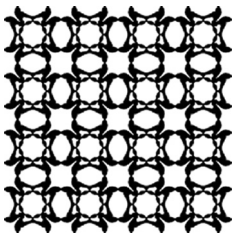	$\begin{bmatrix} 50.12 & -29.04 & 0.00 \\ -29.04 & 50.12 & 0.00 \\ 0.00 & 0.00 & 4.32 \end{bmatrix}$ $\mu_{12} = \mu_{21} = -0.58$
With curvature constraint κ_{max}=1	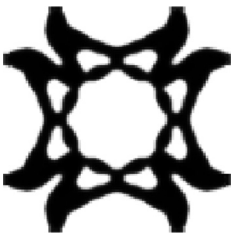	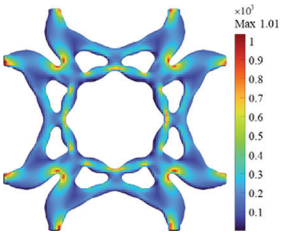	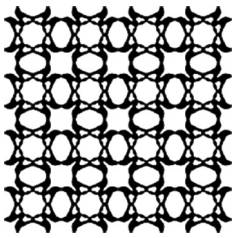	$\begin{bmatrix} 53.73 & -25.98 & 0.00 \\ -25.98 & 53.73 & 0.00 \\ 0.00 & 0.00 & 5.69 \end{bmatrix}$ $\mu_{12} = \mu_{21} = -0.48$
With curvature constraint κ_{max}=0.8	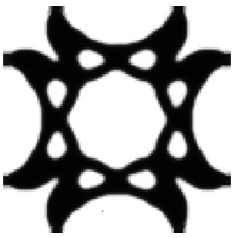	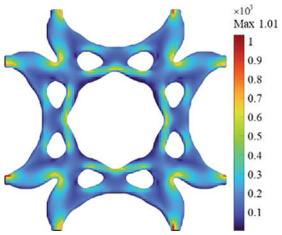	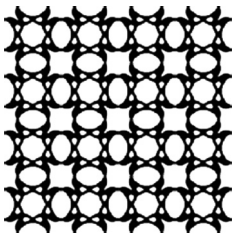	$\begin{bmatrix} 61.55 & -11.31 & -0.03 \\ -11.31 & 61.55 & -0.07 \\ -0.03 & -0.07 & 7.00 \end{bmatrix}$ $\mu_{12} = \mu_{21} = -0.18$
With curvature constraint κ_{max}=0.7	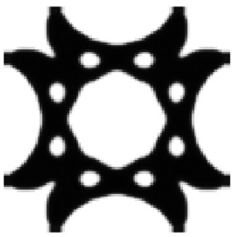	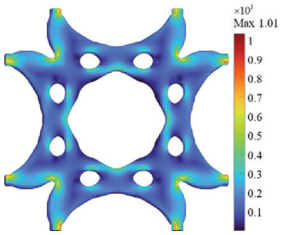	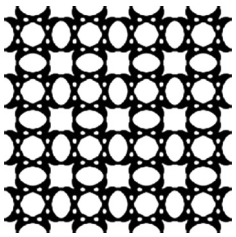	$\begin{bmatrix} 68.33 & -1.01 & -0.00 \\ -1.01 & 68.33 & -0.00 \\ -0.00 & -0.00 & 10.04 \end{bmatrix}$ $\mu_{12} = \mu_{21} = -0.01$

Among all the results applied with curvature constraints, the joints at the microstructure boundaries are reinforced, demonstrating that the density stitching method proposed in Figure 1 can realize the accurate evaluation of negative curvatures at the boundary, taking full consideration of structural periodicity.

3.2. 2D case 2: Anisotropic NPR microstructures

For 2D case 2, the volume constraint of all anisotropic NPR microstructures was set at f_v = 25%. Three comparative scenarios were examined: (i) microstructure without curvature constraint, (ii) microstructure with a negative curvature constraint of κ_{max} = 1, and (iii) microstructure with a negative curvature constraint of κ_{max} = 0.5.

The optimization results are summarized in Table 2. For the NPR microstructure without curvature constraint, the maximum negative curvature reached κ_{max} = 1.9. In this case, the anisotropic microstructures do not rely on numerous flexible hinges to achieve NPR, as shown in case 1. Instead, its auxetic behavior is determined by the re-entrant geometry, yielding NPR of μ_{12} = −1.79 and μ_{12} = −0.45. Stress analysis shows that stress is concentrated at re-entrant corners, with a peak of 0.81×10³ MPa. For the anisotropic NPR microstructures with maximum negative curvature constraints of κ_{max} = 1 and κ_{max} = 0.5, the sharp re-entrant corners are optimized, and the stress concentration is alleviated. Similar to the conclusion in case 1, the NPR performance decreases with the

Table 2. Comparison of anisotropic NPR microstructures under different curvature constraints

Isotropic NPR microstructures	Base cell	Von Mises stress distribution under simultaneously applied unit test strains	4×4 unit cells	Properties D^H μ_{12} μ_{21}
Without curvature constraint $\kappa_{max} = 0.9$	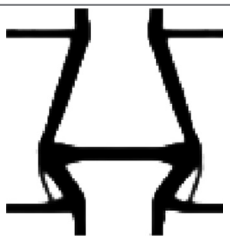	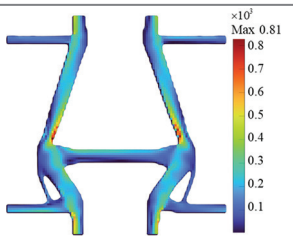	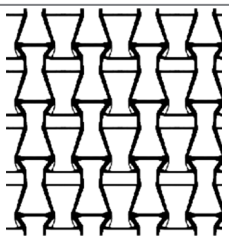	$\begin{bmatrix} 15.11 & -27.00 & 0.00 \\ -27.00 & 60.13 & 0.01 \\ 0.00 & 0.01 & 0.45 \end{bmatrix}$ $\mu_{12} = -1.79$ $\mu_{21} = -0.45$
With curvature constraint $\kappa_{max} = 1$		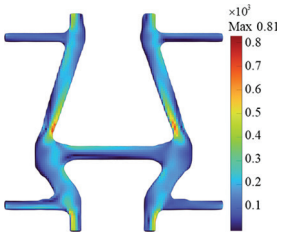	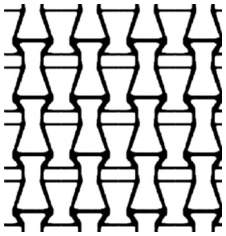	$\begin{bmatrix} 15.30 & -25.40 & 0.00 \\ -25.40 & 60.81 & 0.00 \\ 0.00 & 0.00 & 0.46 \end{bmatrix}$ $\mu_{12} = -1.66$ $\mu_{21} = -0.42$
With curvature constraint $\kappa_{max} = 0.5$		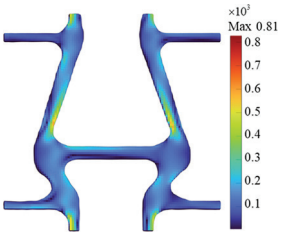		$\begin{bmatrix} 15.49 & -23.52 & 0.00 \\ -23.52 & 61.08 & 0.01 \\ 0.00 & 0.01 & 0.46 \end{bmatrix}$ $\mu_{12} = -1.52$ $\mu_{21} = -0.39$

Abbreviation: NPR: Negative Poisson's ratio.

enhancement of curvature constraint, whereas the tensile–compressive stiffness of the structure is enhanced.

3.3. 2D case 3: Chiral NPR microstructures

For 2D case 3, the volume constraint of all chiral NPR microstructures was set at f_v = 25%. Three comparative scenarios were examined: (i) microstructure without curvature constraint, (ii) microstructure with a negative curvature constraint of κ_{max} = 1, and (iii) microstructure with a negative curvature constraint of κ_{max} = 0.5.

The optimization results are summarized in Table 3. For the NPR microstructure without curvature constraint, the maximum negative curvature reached κ_{max} = 1.9, and the maximum von Mises stress is 0.93×10³ MPa. For the chiral metamaterial in case 3, its NPR effect does not primarily rely on flexible hinges but rather on the re-entrant geometry. Consequently, under curvature constraints, the stress distribution is improved, whereas the μ_{12} of the Poisson's ratios decreases slightly from −0.81 to −0.79 and −0.77. The conclusions for the chiral NPR microstructure under curvature constraints are consistent with those in case 1 and case 2: As the negative curvature constraint increases, the NPR performance declines, whereas the tensile–compressive stiffness is enhanced and the stress distribution is improved.

3.4. 3D case 1: Anisotropic NPR microstructures

For 3D case 1, the volume constraint of all anisotropic NPR microstructures was set at f_v = 40%. Two comparative scenarios were examined: (i) microstructure without curvature constraint, and (ii) microstructure with a negative curvature constraint of κ_{max} = 1.

The optimization results are summarized in Figure 5. For the NPR microstructure without curvature constraint, the maximum negative curvature reached κ_{max} = 2.2. This microstructure is similar to the 2D case 1, whereas its auxetic behavior mainly relies on the deformation of numerous flexible hinges. As a result, stress concentrations occur at the flexible hinges as shown in Figure 5D, and the maximum stress reaches 4.26×10³ MPa. When the maximum curvature constraint κ_{max} = 1 is applied, the sharp corners of the flexible hinges are smoothed, and the maximum stress at the hinges is reduced, as shown in Figure 5J (for better observation and comparison, the upper limit of the scale bar for stresses was set to 4.26×10³ MPa). The tensile–compressive stiffness in all

Table 3. Comparison of chiral NPR microstructures under different curvature constraints

Chiral NPR microstructures	Base cell	Von Mises stress distribution under simultaneously applied unit test strains	4×4 unit cells	Properties D^H μ_{12} μ_{21}
Without curvature constraint κ_{max}=1.8		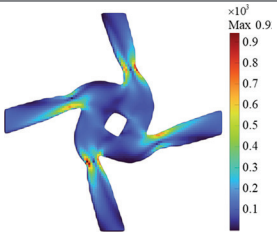	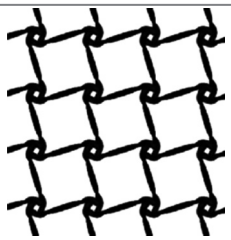	$\begin{bmatrix} 32.52 & -26.40 & 8.71 \\ -26.40 & 33.33 & -8.90 \\ 8.71 & -8.90 & 4.35 \end{bmatrix}$ $\mu_{12} = -0.81$ $\mu_{21} = -0.79$
With curvature constraint κ_{max}=1		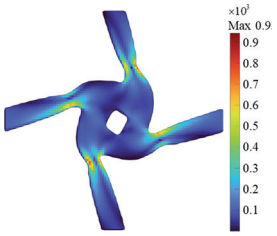	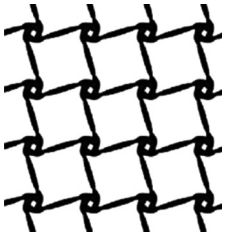	$\begin{bmatrix} 33.33 & -26.41 & 8.52 \\ -26.41 & 34.12 & -8.73 \\ 8.52 & -8.73 & 3.26 \end{bmatrix}$ $\mu_{12} = -0.79$ $\mu_{21} = -0.77$
With curvature constraint κ_{max}=0.5		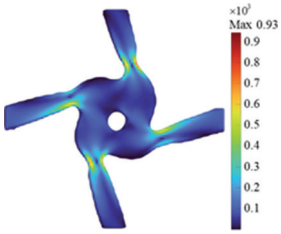	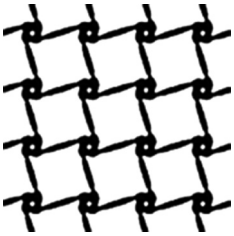	$\begin{bmatrix} 34.33 & -26.51 & 8.72 \\ -26.51 & 35.47 & -9.10 \\ 8.72 & -9.10 & 2.91 \end{bmatrix}$ $\mu_{12} = -0.77$ $\mu_{21} = -0.75$

Abbreviation: NPR: Negative Poisson's ratio.

directions are improved. However, with μ_{13} and μ_{31} of the Poisson's ratios approaching 0, the NPR effect in the 1–3 direction is nearly eliminated.

3.5. 3D case 2: anisotropic NPR microstructures

For 3D case 2, the volume constraint of all anisotropic NPR microstructures was set at f_v = 40%. Two comparative scenarios were examined: (i) microstructure without curvature constraint, and (ii) microstructure with a negative curvature constraint of κ_{max} = 1.

The optimization results are summarized in Figure 6. For the NPR microstructure without curvature constraint, the maximum negative curvature reached κ_{max} = 1.9. Unlike the 3D case 1, this microstructure does not rely on numerous flexible hinges. Instead, its auxetic behavior is achieved through the re-entrant geometry. Upon the application of the negative curvature constraint κ_{max} = 1, improvements are observed in both the sharp concave regions and the stress distribution of the microstructure, which is consistent with the earlier conclusions. Notably, as the deformation of this microstructure is not predominantly governed by flexible hinges, its NPR effect is effectively retained.

3.6. Simulation and experiment

In this section, we used all 2D cases and 3D case 2 as simulation and experimental objects to systematically investigate the mechanical properties of NPR metamaterials with negative curvature constraint. All experimental specimens were fabricated by Formlabs FORM 3L stereolithography 3D printer (Formlabs Inc., USA) to mitigate the anisotropy induced by the manufacturing process. The layer thickness of 0.1 mm was adopted, and the postprocessing procedure consisted of isopropanol immersion for 120 min and ultraviolet (UV) curing at 60°C for 180 min. A more detailed view of the microstructures' deformation process can be found within the experimental video provided in the supplementary materials.

The 2D simulation and the corresponding experimental results are presented in Figure 7. For all 2D NPR metamaterials' simulation, we applied a fully fixed constraint at the bottom of the structure and a uniform tensile force of F = 10N on the top. Under the same tensile force, the maximum displacement of all NPR metamaterials without curvature constraint is larger than that of curvature-constrained designs, which proves that the curvature constraint enhances the tensile

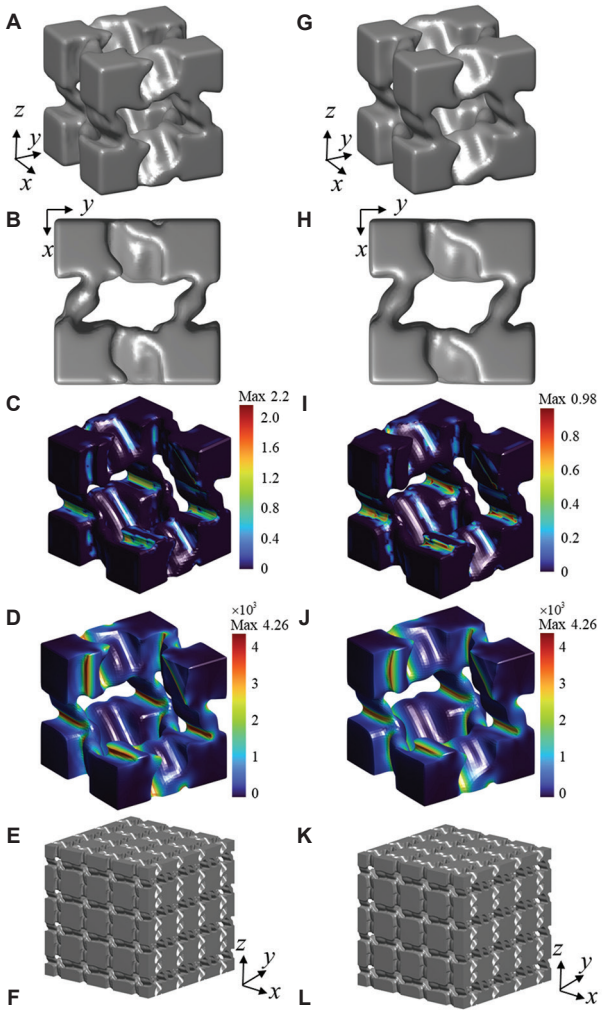

Figure 5. Comparison of 3D case 1 NPR microstructures under different curvature constraints for microstructure without curvature constraint (A-F) and for microstructure with curvature constraint κ_{max} = 1 (G-L). (A and G) Base cell; (B and H) Top view of base cell; (C and I) Negative curvature distribution (display 7/8 microstructure); (D and J) Von Mises stress distribution under simultaneously applied unit test strains (display 7/8 microstructure); (E and K) 4×4 unit cells; (F and L) Properties
Abbreviation: NPR: Negative Poisson's ratio

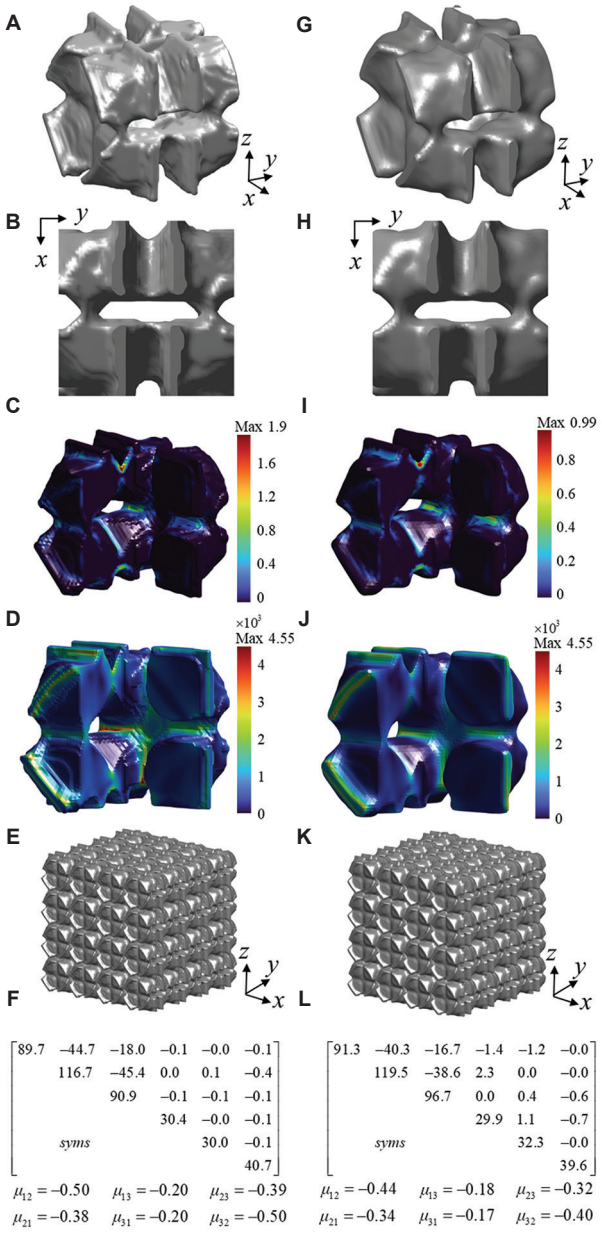

Figure 6. Comparison of 3D case 2 NPR microstructures under different curvature constraints for microstructure without curvature constraint (A-F) and for microstructure with curvature constraint κ_{max} = 1 (G-L). (A and F) Base cell; (B and G) Top view of base cell; (C and I) Negative curvature distribution (display 3/4 microstructure); (D and J) Von Mises stress distribution under simultaneously applied unit test strains (display 3/4 microstructure); (E and K) 4×4 unit cells; (F and L) Properties
Abbreviation: NPR: Negative Poisson's ratio

stiffness of metamaterials. In the experiments on 2D chiral metamaterials and 2D anisotropic metamaterials (corresponding to Figure 7G-H and K-L), it is evident that the microstructures optimized with curvature constraints can resist larger deformation. Specifically, curvature constraints can enhance the total energy absorption capability and postpone the initiation of failure for these two types of microstructures. For an isotropic microstructure, a strong curvature constraint leads to a quasi-zero Poisson's ratio of the microstructure, but its elongation before failure is only slightly improved (Figure 7C and D).

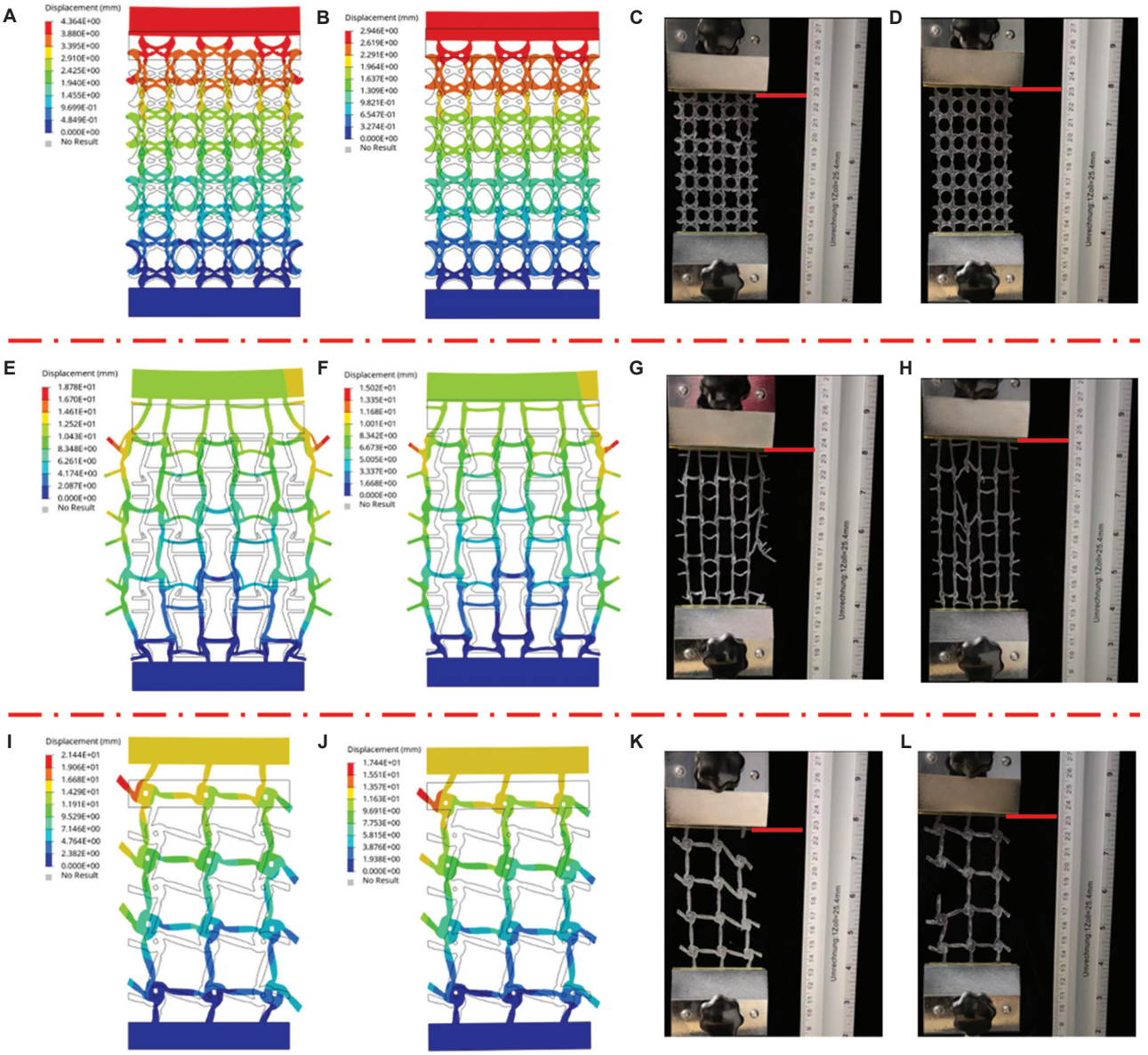

Figure 7. Simulation and experimental diagrams of 2D NPR metamaterials. (A) Simulation of isotropic NPR metamaterial without curvature constraint; (B) Simulation of isotropic NPR metamaterial with curvature constraint κ_{max} = 0.7; (C) Experiment of isotropic NPR metamaterial without curvature constraint; (D) Experiment of isotropic NPR metamaterial without curvature constraint κ_{max} = 0.7; (E) Simulation of anisotropic NPR metamaterial without curvature constraint; (F) Simulation of anisotropic NPR metamaterial with curvature constraint κ_{max} = 0.5; (G) Experiment of anisotropic NPR metamaterial without curvature constraint; (H) Experiment of anisotropic NPR metamaterial without curvature constraint κ_{max} = 0.5; (I) Simulation of chiral NPR metamaterial without curvature constraint; (J) Simulation of chiral NPR metamaterial with curvature constraint κ_{max} = 0.5; (K) Experiment of chiral NPR metamaterial without curvature constraint; (L) Experiment of chiral NPR metamaterial without curvature constraint κ_{max} = 0.5
Abbreviation: NPR: Negative Poisson's ratio

For 3D case 2, the anisotropic NPR metamaterials without curvature constraint/with κ_{max} = 1 curvature constraint, we applied compression load of F = 100N on the x, y, and z surfaces, respectively. The simulation results are shown in Figure 8, and we can draw the same conclusions as obtained previously. The NPR metamaterials exhibit a compressive contraction effect in all directions, regardless of whether curvature constraint is applied. When the curvature constraint is introduced, the compressive stiffness of the metamaterial is enhanced, whereas its NPR effect is slightly weakened.

In Figure 9, we present a comparison of the additive manufacturing results. It can be observed that the microstructures with negative curvature constraint

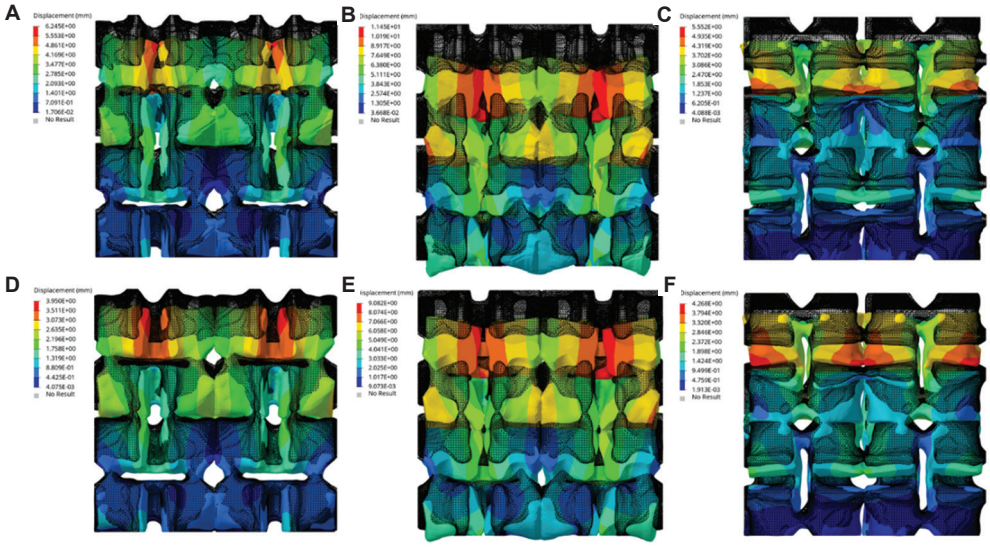

Figure 8. Simulation diagrams of 3D anisotropic NPR metamaterials for metamaterials without curvature constraint (A-C) and for metamaterials with curvature constraint $\kappa_{max} = 1$ (D-F). (A and D) z-direction compression simulation; (B and E) x-direction compression simulation; (C and F) z-direction compression simulation
Abbreviation: NPR: Negative Poisson's ratio

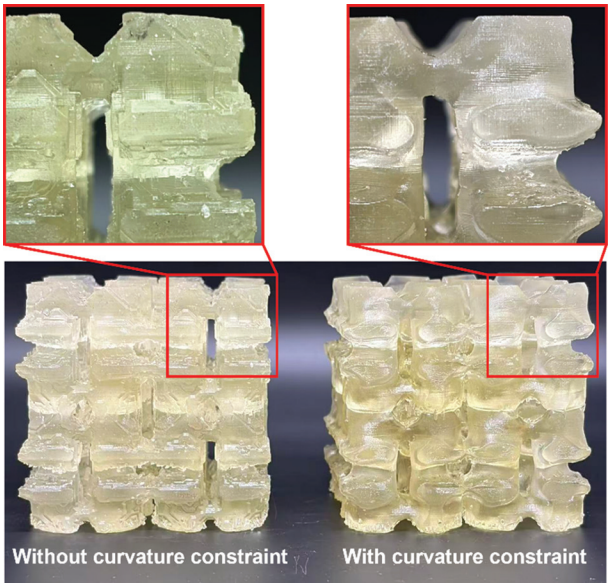

Figure 9. Comparison of optimized 3D NPR metamaterials
Abbreviation: NPR: Negative Poisson's ratio

have smooth concave regions, which can effectively alleviate stress concentration. In Figure 10, we present a comparison of the compression experiments. During the tests, the 3D metamaterial does not collapse directly but instead exhibits a typical compressive expansion behavior after the compressive contraction stage. Therefore, only the data from the compression contraction stage were selected for drawing the force-displacement curves. We conducted five sets of parallel experiments, and the force-displacement curves with standard deviation error bars are presented in Figure 10E. Based on the mean values of the experimental data, the energy absorption capability of the NPR microstructure with curvature constraint (2.592J) is enhanced by 39.13% compared to that without curvature constraints (1.863J).

4. Discussion

As illustrated by the five cases in Section 3, sharp corners inside the NPR microstructures can be effectively smoothed by introducing the negative curvature constraint, leading to the alleviation of stress concentration. The strengthening of the curvature constraint leads to an increase in tensile–compressive stiffness; however, it compromises the auxetic effect.

It is also worth noting that the deformation of NPR microstructures obtained through TO mainly relies on flexible hinges or re-entrant features. For microstructures whose deformation is dominated by flexible hinges, curvature constraints will significantly reduce the NPR effect, whereas for those governed by re-entrant features, the NPR performance can be largely preserved under curvature constraints. This phenomenon is similar to previous findings in compliant mechanisms[47]: Hinge-based deformation corresponds to local compliance,[48,49] whereas re-entrant geometry-based deformation represents global compliance.[50-52] Consequently, optimizing flexible hinges tends to impair the deformation performance of the structure.

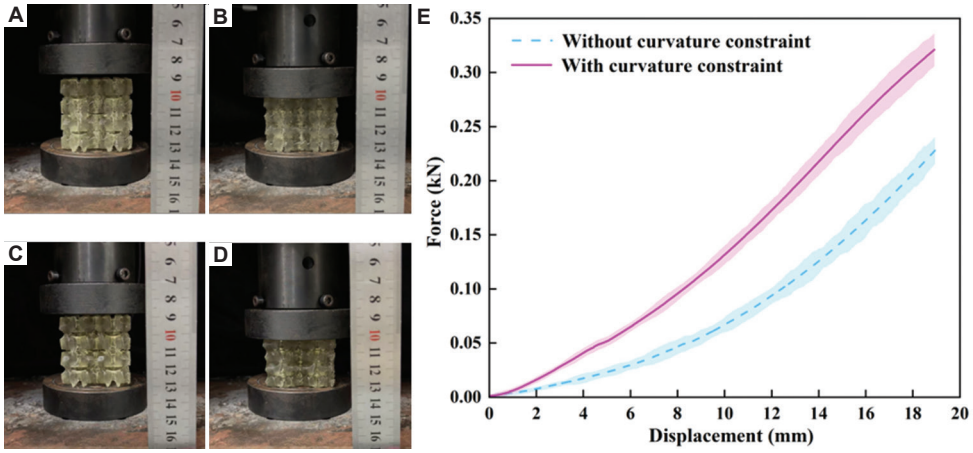

Figure 10. Experiment results of 3D NPR metamaterials. (A and B) Initial (A) and compression state (B) of metamaterials without curvature constraint; (C and D) Initial (C and D) compression state of metamaterials with curvature constraint $\kappa_{max} = 1$; (E) Force–displacement curves
Abbreviation: NPR: Negative Poisson's ratio

As observed in the experiments presented in Section 3 and supplementary materials, the selection of appropriate curvature constraint improves the energy absorption capability and deformability of the microstructure. Overly constraining the curvatures may eliminate the NPR effect. However, due to the varying types of microstructures—depending on flexible hinges or re-entrant configurations for large deformation—the current study still faces challenges in universally configuring the curvature constraint to balance the deformability, energy absorption, and NPR effect. This issue should be addressed in future research.

5. Conclusion

To avoid the stress-concentrated sharp turnings commonly observed in TO-designed NPR microstructures, this study proposes a B-DGTO framework with the curvature constraint to mitigate stress concentrations at flexible hinges and re-entrant features. The B-DGTO framework establishes a derivable SDF from the density-based topological field, enabling the accurate evaluation and constraining of curvatures along density boundaries through the finite difference operations using a level-set approach. The most negative curvatures are effectively constrained to below the thresholds, and the accordingly designed NPR microstructures are manufactured by 3D printing for demonstration and tests. Both numerical and experimental results validate the effectiveness of the proposed method on various NPR configurations, including isotropic NPR microstructures, anisotropic NPR microstructures, and chiral NPR microstructures. In addition, the distinct influences of the curvature constraint on auxetic performance of the flexible hinge and re-entrant feature-based NPR microstructures are discussed in detail, providing insights for the appropriate application of the curvature constraint.

Acknowledgments

None.

Funding

The authors would like to acknowledge the financial support from the National Natural Science Foundation of China (grant number 52475290).

Conflict of interest

Jikai Liu serves as the Editorial Board Member of the journal, but did not in any way involve in the editorial and peer-review process conducted for this paper, directly or indirectly. Other authors declare they have no competing interests.

Author contributions

Conceptualization: Kaixian Liang, Jikai Liu
Formal analysis: Chengxiang Liu
Investigation: Kaixian Liang, Jikai Liu
Methodology: All authors
Writing–original draft: Kaixian Liang
Writing–review & editing: Jikai Liu

Ethics approval and consent to participate

Not applicable.

Consent for publication

Not applicable.

Availability of data

The data that support the findings of this study are available from the corresponding author upon reasonable request.

References

1. Lakes R. Foam structures with a negative Poisson's ratio. *Science*. 1987;235(4792):1038-1040.

   doi: 10.1126/science.235.4792.1038

2. Kolken HM, Zadpoor A. Auxetic mechanical metamaterials. *RSC Adv*. 2017;7(9):5111-5129.

   doi: 10.1039/c6ra27333e

3. Saxena KK, Das R, Calius EP. Three decades of auxetics research- materials with negative Poisson's ratio: A review. *Adv Eng Mater*. 2016;18(11):1847-1870.

   doi: 10.1002/adem.201600053

4. Li F, Zhang Q, Wang Z, Zhu D. A new three-dimensional re-entrant negative Poisson's ratio metamaterial with tunable stiffness. *Eng Struct*. 2024;306:117793.

   doi: 10.1016/j.engstruct.2024.117793

5. Choi J, Lakes R. Fracture toughness of re-entrant foam materials with a negative Poisson's ratio: Experiment and analysis. *Int J Fract*. 1996;80(1):73-83.

   doi: 10.1007/bf00036481

6. Li F, Chen Y, Zhu D. Revealing the sound transmission loss capacities of sandwich metamaterials with re-entrant negative Poisson's ratio configuration. *Materials*. 2023;16(17):5928.

   doi: 10.3390/ma16175928

7. Wen G, Zhang S, Wang H, *et al*. Origami-based acoustic metamaterial for tunable and broadband sound attenuation. *Int J Mech Sci*. 2023;239:107872.

   doi: 10.1016/j.ijmecsci.2022.107872

8. Liu W, Wang N, Luo T, Lin Z. In-plane dynamic crushing of re-entrant auxetic cellular structure. *Mater Design*. 2016;100:84-91.

   doi: 10.1016/j.matdes.2016.03.086

9. Tian J, Yang J, Zhao Y. Metamaterial with synergistically controllable Poisson's ratio and thermal expansion coefficient. *Int J Mech Sci*. 2023;256:108488.

   doi: 10.1016/j.ijmecsci.2023.108488

10. He H, Niu X, Xu Z, *et al*. Interdigitated structure-derived scalable all-solid-state electrocaloric cooling device using lead-free BaSrTiO3-based multilayer ceramics. *Joule*. 2025;9(10):102128.

    doi: 10.1016/j.joule.2025.102128

11. Wei K, Peng Y, Qu Z, Pei Y, Fang D. A cellular metastructure incorporating coupled negative thermal expansion and negative Poisson's ratio. *Int J Solids Struct*. 2018;150:255-267.

    doi: 10.1016/j.ijsolstr.2018.06.018

12. Zhang Q, Li F, Zhu D, Zhang T, Chen L. Quasi-static and impact performance study of a three-dimensional negative Poisson's ratio structure with adjustable mechanical properties. *Int J Impact Eng*. 2024;193:105057.

    doi: 10.1016/j.ijimpeng.2024.105057

13. Kun Y, Fei T, Bo WY, He HY. Study on impact energy absorption performance and optimization of negative Poisson's ratio structure. *J Braz Soc Mech Sci Eng*. 2023;45(6):328.

    doi: 10.1007/s40430-023-04253-3

14. Qin S, Deng X, Yang F, Lu Q. Energy absorption characteristics and negative Poisson's ratio effect of axisymmetric tetrachiral honeycombs under in-plane impact. *Compos Struct*. 2023;323:117493.

    doi: 10.1016/j.compstruct.2023.117493

15. Bertoldi K, Vitelli V, Christensen J, Van Hecke M. Flexible mechanical metamaterials. *Nat Rev Mater*. 2017;2(11):17066.

    doi: 10.1038/natrevmats.2017.66

16. Surjadi JU, Gao L, Du H, *et al*. Mechanical metamaterials and their engineering applications. *Adv Eng Mater*. 2019;21(3):1800864.

    doi: 10.1002/adem.201800864

17. Zhai Z, Wu L, Jiang H. Mechanical metamaterials based on origami and kirigami. *Appl Phys Rev*. 2021;8(4):041319.

    doi: 10.1063/5.0051088

18. Bendsøe MP, Sigmund O. *Topology Optimization: Theory, Methods, and Applications*. Germany: Springer Science and Business Media; 2003.

19. Allaire G, Jouve F, Toader AM. A level-set method for shape optimization. *C R Mathématique*. 2002;334(12):1125-1130.

    doi: 10.1016/s1631-073x(02)02412-3

20. Wang MY, Wang X, Guo D. A level set method for structural topology optimization. *Comput Methods Appl Mech Eng*. 2003;(192):227-246.

    doi: 10.1016/s0045-7825(02)00559-5

21. Huang X, Xie M. *Evolutionary Topology Optimization of Continuum Structures: Methods and Applications*. New Jersey, U.S: John Wiley and Sons; 2010.

22. Guo X, Zhang W, Zhong W. Doing Topology Optimization Explicitly and Geometrically-A New Moving Morphable Components Based Framework. *J Appl Mech*. 2014;81(8):081009.

    doi: 10.1115/1.4027609

23. Sigmund O. Materials with prescribed constitutive parameters: An inverse homogenization problem. *Int J Solids Struct*. 1994;31(17):2313-2329.

    doi: 10.1016/0020-7683(94)90154-6

24. Schwerdtfeger J, Wein F, Leugering G, *et al*. Design of

auxetic structures via mathematical optimization. *Adv Mater*. 2011;23(22):2650.

doi: 10.1002/adma.201004090

25. Han Z, Wei K. Multi-material topology optimization and additive manufacturing for metamaterials incorporating double negative indexes of Poisson's ratio and thermal expansion. *Addit Manuf*. 2022;54:102742.

doi: 10.1016/j.addma.2022.102742

26. Bao Y, Wei Z, Jia Z, *et al*. Mechanical metamaterial design with the customized low-frequency bandgap and negative Poisson's ratio via topology optimization. *Extreme Mech Lett*. 2024;67:102124.

doi: 10.1016/j.eml.2024.102124

27. Andreassen E, Lazarov BS, Sigmund O. Design of manufacturable 3D extremal elastic microstructure. *Mech Mater*. 2014;69(1):1-10.

doi: 10.1016/j.mechmat.2013.09.018

28. Li H, Luo Z, Gao L, Walker P. Topology optimization for functionally graded cellular composites with metamaterials by level sets. *Comput Methods Appl Mech Eng*. 2018;328:340-364.

doi: 10.1016/j.cma.2017.09.008

29. Zhang H, Luo Y, Kang Z. Bi-material microstructural design of chiral auxetic metamaterials using topology optimization. *Compos Struct*. 2018;195:232-248.

doi: 10.1016/j.compstruct.2018.04.058

30. Wang C, Zhao H, Wang Y, *et al*. Topology optimization of chiral metamaterials with application to underwater sound insulation. *Appl Math Mech*. 2024;45(7):1119-1138.

doi: 10.1007/s10483-024-3162-8

31. Chen W, Huang X. Topological design of 3D chiral metamaterials based on couple-stress homogenization. *J Mech Phys Solids*. 2019;131:372-386.

doi: 10.1016/j.jmps.2019.07.014

32. Zhou Y, Gao L, Li H. Topology optimization design of graded infills for 3D curved volume by a conformal sweeping method. *Comput Methods Appl Mech Eng*. 2023;412:116009.

doi: 10.1016/j.cma.2023.116009

33. Zhou Y, Gao L, Li H. A ready-to-manufacture optimization design of 3D chiral auxetics for additive manufacturing. *Eng Comput Germany*. 2024;40(3):1517-1538.

doi: 10.1007/s00366-023-01880-1

34. Bernard AR, Yalcin MM, Elsayed MSA. Shape transformers for crashworthiness of additively manufactured engineering resin lattice structures: Experimental and numerical investigations. *Mech Mater*. 2024;190:104925.

doi: 10.1016/j.mechmat.2024.104925

35. Ni Z, Cheng W, Wang Y, *et al*. Topology optimization of two-scale hierarchical structures with high-cycle fatigue resistance. *Comput Methods Appl Mech Eng*. 2024;430:117213.

doi: 10.1016/j.cma.2024.117213

36. Xu S, Liu J, He D, Tang K, Yaji K. Self-support structure topology optimization for multi-axis additive manufacturing incorporated with curved layer slicing. *Comput Methods Appl Mech Eng*. 2025;438:117841.

doi: 10.1016/j.cma.2025.117841

37. Guo Y, Xu S, Wang Y, *et al*. DGTO: Derivable geodesics-coupled topology optimization for multi-axis hybrid additive and subtractive manufacturing with curved layer generation. *Addit Manuf*. 2025;105:104786.

doi: 10.1016/j.addma.2025.104786

38. Liang K, Liu J, Xu S, Guo Y. DGTO: Derivable geodesics-coupled topology optimization for multi-axis 3D printing of continuous fiber-reinforced spatial structures. *Comput Methods Appl Mech Eng*. 2026;448:118419.

doi: 10.1016/j.cma.2025.118419

40. Osher S, Fedkiw RP. *Level Set Methods and Dynamic Implicit Surfaces*. Vol 1. New York: Springer; 2005.

41. Crane K, Weischedel C, Wardetzky M. Geodesics in heat: A new approach to computing distance based on heat flow. *ACM Trans Graph (TOG)*. 2013;32(5):1-11.

doi: 10.1145/2516971.2516977

42. Huang J, Liu J. Derivable skeletons in topology optimization for length scale control. *Comput Methods Appl Mech Eng*. 2024;421:116778.

doi: 10.1016/j.cma.2024.116778

43. Wang FW, Lazarov BS, Sigmund O. On projection methods, convergence and robust formulations in topology optimization. *Struct Multidiscip O*. 2011;43(6):767-784.

doi: 10.1007/s00158-010-0602-y

44. Bartz R, Franke T, Fiebig S, Vietor T. Density-based shape optimization of 3D structures with mean curvature constraints. *Struct Multidiscip O*. 2022;65:5.

doi: 10.1007/s00158-021-03089-6

45. Xia L, Breitkopf P. Design of materials using topology optimization and energy-based homogenization approach in Matlab. *Struct Multidiscip O*. 2015;52(6):1229-1241.

doi: 10.1007/s00158-015-1294-0

46. Svanberg K. The method of moving asymptotes-a new method for structural optimization. *Int J Numer Meth Eng*. 1987;24(2):359-373.

48. Lazarov BS, Sigmund O. Filters in topology optimization based on Helmholtz-type differential equations. *Int J Numer Meth Eng*. 2011;86(6):765-781.

doi: 10.1002/nme.3072

49. Zhu B, Zhang X, Zhang H, *et al*. Design of compliant mechanisms using continuum topology optimization: A review. *Mech Mach Theory*. 2020;143:103622.

doi: 10.1016/j.mechmachtheory.2019.103622

50. Jin M, Zhang X, Zhu B, Wang N. Spring-joint method for topology optimization of planar passive compliant mechanisms. *Chin J Mech Eng*. 2013;26(6):1063-1072.

doi: 10.3901/cjme.2013.06.1063

51. Jin M, Zhang X, Zhu B. A numerical method for static analysis of pseudo-rigid-body model of compliant mechanisms. *Proc Inst Mech Eng Part C J Mech Eng Sci*. 2014;228(17):3170-3177.

doi: 10.1177/0954406214525951

52. Zhu B, Zhang X, Fatikow S. Level set-based topology optimization of hinge-free compliant mechanisms using a two-step elastic modeling method. *J Mech Design*. 2014;136(3):031007.

doi: 10.1115/1.4026097

53. Liang K, Zhu D, Liu J. Topology optimization of a spatial compliant parallel mechanism based on constant motion transmission characteristic matrix. *Mech Mach Theory*. 2023;180:180105125.

doi: 10.1016/j.mechmachtheory.2022.105125

54. Jin M, Zhang X. A new topology optimization method for planar compliant parallel mechanisms. *Mech Mach Theory*. 2016;95:42-58.

doi: 10.1016/j.mechmachtheory.2015.08.016

Appendix

Table A1. Nomenclature: Symbols and values used in this research

Symbol	Value	Description
$E_{micro}^{\min}$	1e-9	Elastic modulus of void domain
E_{micro}^{0}	1000	Elastic modulus of based material
p	3	Penalization parameter
h_0	1	Thermal conductivity coefficient of solid domain
h_{min}	1e-3	Thermal conductivity coefficient of void domain
β_s	100	Sharpness of the sigmoid function
P	18	P-norm
η	0.5	Threshold of the Heaviside function
D^{H}		Effective elasticity tensor of microstructure
D_{ijkl}^{H}		Component of elasticity tensor
Y		Volume of the periodic unit cell
D_{pqrs}		Elastic tensor component of based material
ε_{pq}^{0}		Unit test strain
ε_{pq}^{*}		Response strain
υ		Virtual displacement
$\mathrm{u}_{\mathrm{n}}^{\mathrm{A}}$		Element displacement
ρ		Design variable
$\bar{\rho}$		Design variable after PDE filtering
$\tilde{\bar{\rho}}$		Design variable after PDE filtering and Heaviside projection
$\hat{\rho}$		Density after boundary stitching
k_{micro}^{0}		Element stiffness matrix of based material with unit Young's modulus
k_{n}		Element stiffness matrix after density interpolation
Q_0		Element transient thermal conductivity matrix
A		Assembly matrix for global thermal conductivity matrix
Q		Global thermal conductivity matrix
T		Temperature field
b		Heat load
ω		Normalized temperature gradient field
L		Laplacian matrix
φ		Signed distance function
κ		Mean curvature
κ_{max}		Upper bound of mean curvature
δ		Maximum curvature constraint defined by the P-norm
V		Solid volume of a unit cell
V_0		Volume of a unit cell
f_v		Upper bound of volume fraction